TOWARDS A MULTISCALE RHEOLOGICAL MODEL OF FRESH CEMENT PASTES: A POPULATION BALANCE APPROACH

Juan Pablo Gallo-Molina[a,*],Karel Lesage[b] and Ingmar Nopens[a]

[a] BIOMATH, Department of Data Analysis and Mathematical Modelling, Ghent University, Ghent, Belgium.
[b] Magnel-Vandepitte Laboratory, Department of Structural Engineering and Building Materials, Ghent University, Ghent, Belgium.
[*] Corresponding author. Email address: JuanPablo.GalloMolina@UGent.be

Abstract

In its fresh state, cement - the hydraulic binder responsible for the hardening of concrete - is a highly concentrated suspension in which nano and mesoscopic phenomena and their interactions determine its macroscopic rheological behaviour. This complexity creates significant challenges in the modelling of the material. In this work, a multiscale modelling framework capable of predicting rheological quantities of early age fresh cement pastes is proposed. Molecular Dynamics was used to obtain a high resolution picture of the colloidal interactions and their dependence on chemical composition. This information was subsequently scaled up and used within the aggregation and breakage kernels of a population balance model, which is then used to deduce rheological responses. Rheological, granulometric and spectroscopic measurements were performed to test and inform the model. Differences in the chemical composition of the studied samples could be used to produce satisfactory predictions of the observed viscosity curves.

Keywords: Cement, PBM, Molecular Dynamics, rheology.

1. Introduction

Concrete is the one of the most produced materials in the world and it is a crucial part of infrastructure projects across the globe. Consequently, its usage comes with enormous economic and environmental implications. Among others, its life cycle has been associated with as much as 8% of all man made carbon dioxide emissions (Flatt et al., 2012). As a result, the industry has been transitioning towards the use of non-traditional aggregates and chemical admixtures. Likewise, a reduction in the overall quantity of cement (the hydraulic binder that allows the material to harden) employed in a given application has been championed as a way forward. This, however, has spawned a series of engineering challenges.

Rheology control is one of these challenges. It arises immediately after water is added to a concrete mixture and it cannot be disregarded even though it must be considered only during the first few hours of a life cycle that usually encompasses years or decades. The reason is that the rheological properties of fresh concrete are critical for a series of fundamental steps such as mixture design and initial placing. They also play and important role in

the eventual structural performance of the hardened material (Chidiac & Mahmoodzadeh, 2009). It is for this reason the industry is rapidly approaching a new consensus: the information provided by traditional empirical testing methods is no longer sufficient. Consequently, the implementation of mechanistic models with reliable predictive power is seen as a new goalpost.

This poses yet another challenge, since the rheological behaviour of these systems is determined by a complex set of interactions that encompass several length scales (Flatt, 2004a, 2004b; Flatt & Bowen, 2007; Roussel, 2007; Roussel et al., 2007, 2010). Modelling therefore must consider this reality in some capacity. Accordingly, the authors have previously demonstrated the suitability of the population balance framework as the foundation for a mechanistic description of the flow of cement suspensions; cement being arguably the most important component of concrete (Gallo-Molina et al., 2020). This framework is particularly well suited to the system at hand because it allows for the description of the transient evolution of the Particle Size Distribution (PSD) (Ramkrishna, 2000; Yeoh et al., 2014), which drives rheology in concentrated suspensions such as a cement paste (Quemada, 1977, 1998; Roussel et al., 2012).

Another part of the puzzle resides at the nanoscale, as molecular interactions control aggregation and breakage dynamics in these suspensions (Castillo et al., 2012; Flatt, 2004a; Lesko et al., 2001; Nachbaur et al., 1998; Roussel et al., 2010; Uchikawa et al., 1997). These dynamics subsequently determine the way in which the PSD changes, which implies that information regarding these molecular effects shall be present in some way in the aggregation and breakage kernels of the previously alluded population balance based model. Unfortunately, an adequate description of said effects is far from trivial for the reason that some of the parameters required by, for example, the classic DLVO theory (Derjaguin & Landau, 1993; Verwey, 1947) are not currently known. Furthermore, it has been observed that several phenomena present in cementitious systems (e.g., hydration forces) may severely limit the applicability of a continuous approximation of colloidal interactions such as the aforementioned DLVO model (Jönsson et al., 2004; Lesko et al., 2001; Lomboy et al., 2011; Nachbaur et al., 1998; Plassard et al., 2005; van Damme, 2006).

As an alternative, Molecular Dynamics (MD) has been identified as a way of obtaining a high resolution picture of the characteristics of the colloidal interactions present in early age cement pastes (Argyris et al., 2008; Gallo-Molina et al., 2021; Kalinichev et al., 2007; Wang et al., 2004). Indeed, it has been observed that the chemical

composition of the clinker particles can significantly alter the nature of said interactions; a situation that cannot be captured with the currently employed approaches, which rely on treating cement as a chemically analogous substance such as magnesium oxide (Gallo-Molina et al., 2021). The opportunity thus arises to employ both MD and PBM to obtain a more comprehensive description of the rheology of cement.

In light of the above, this work presents a multiscale model based on the PBM framework aimed at predicting rheological observables in early age cement pastes. Here, the methodology described in a previous publication (Gallo-Molina et al., 2020) is enhanced by the information obtained from MD simulations of the most common clinker phases found in cement (i.e., tricalcium silicate (C_3S[1]); dicalcium silicate (C_2S); tricalcium aluminate (C_3A); and calcium aluminoferrite (C_4AF)). This data was used to construct a statistical picture of the effective colloidal interactions among granules, which was then used to formulate aggregation and breakage kernels. The final result is a population balance model capable of predicting the flow curve of a cement paste as a function of its (heterogeneous) chemical composition and other process conditions. To the authors' knowledge this methodology has not previously been described and thus it can constitute a promising path towards the full description concrete rheology.

2. Materials and Methods

Seven clinker samples were obtained from a single product line of a commercial cement manufacturing plant. Figure 1 illustrates the chemical structure of the phases present in the samples.

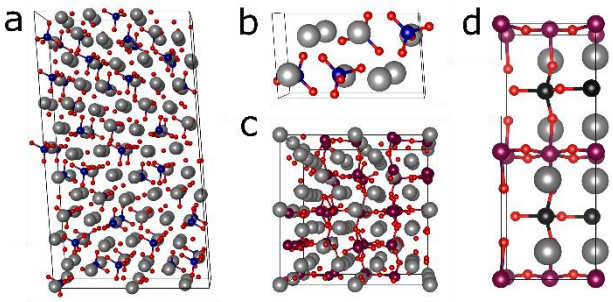

Figure 1. Unit cells of the cement clinker phases present in the studied sample. a) C_3S; b) C_2S; c) C_3A; d) C_4AF. Grey spheres: calcium atoms; blue spheres: silicon atoms; purple spheres: aluminium atoms; red spheres: oxygen atoms; black spheres: iron atoms; green spheres: sulphur atoms; light grey spheres: hydrogen atoms.

[1] Here, cement chemistry industry nomenclature is used: C = CaO, S = SiO_2, H = H_2O, A = Al_2O_3, F = Fe_2O_3.

Approximately 50 g of each clinker was ground in a vibratory disc mill (Aurec S.A.) up to a specific surface area of 0.225 ± 0.030 m^2/g, which was measured by laser granulometry in a Mastersizer 2000S (Malvern). Isopropanol was used as the suspending fluid. This fineness relates well with commercial cements tested under the same conditions. The particle size distribution of the samples was measured using the same laser granulometry setup and it is shown in figure 2. Five consecutive measurements were taken for each sample and the average was subsequently calculated. As seen in the figure, considerable overlap exists among all samples.

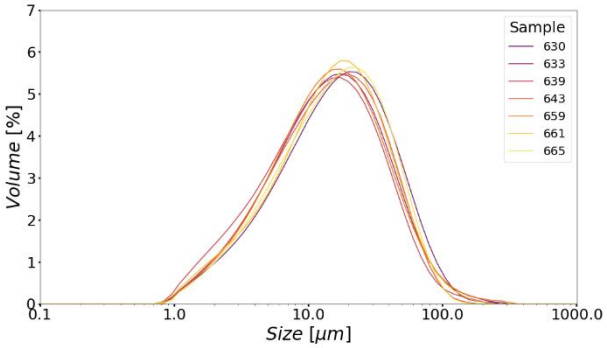

Figure 2. PSD of the ground clinker samples

After grinding, calcium sulphate hemihydrate ($CaSO_4 \cdot 0.5H_2O$) was added to the clinker powder in order to control the setting speed of the cement. For each clinker, the total sulphur content was fixed at 3.14% of the total binder mass. This criterion originated in the commercial manufacturing process.

For the rheological experiments, a constant amount of water was subsequently added to the sulphate enriched clinkers to create cement pastes. A 3 ml paste sample was always hand mixed for 3 min with a water/cement ratio of 0.4. Each sample was left to rest for 60 min before being loaded into the rheometer. A stress controlled MCR 102 rheometer manufactured by Anton Paar was used to perform shear tests on all paste samples. Cross-hatched parallel plates of 50 mm diameter were selected to avoid apparent wall slip during measurements at low shear rates. The gap between the parallel plates was fixed at 1 mm. The shear protocol started with a linearly increasing shear rate ramp from 0 to 140 s^{-1} in 90 seconds. This upper rate was maintained for another 30 s. At 120 s, a step-down protocol was started at 120 s^{-1} with steps of -10 s^{-1} for every 20 s until 60 s^{-1} was reached. For every interval, the final viscosity value was recorded for that shear rate. The entire shear test was repeated three times, with fresh materials being used each time.

The chemical composition on the surfaces of the granules was acquired with Raman spectroscopy. Before the measurements could be commenced, flat sample surfaces with diameters of c.a. 5 cm were prepared from large

clinker granules embedded in epoxy resin. Spectra were collected with a Bruker Optics 'Senterra' dispersive Raman spectrometer equipped with an Olympus BX51 microscope and a 532 nm excitation laser. The laser was automated to follow a square grid measuring 250x250 μm. Every other 10 μm, a point measurement was taken, leading to 625 evenly distributed Raman spectra per sample. Spectral areas were selected in accordance with the work of Liu et al. (2015). Subsequent postprocessing was performed in MATLAB (2021) and a fifth order polynomial baseline correction was implemented. Figure 3 shows the average of the processed spectra over the grids for each one of the analysed clinkers.

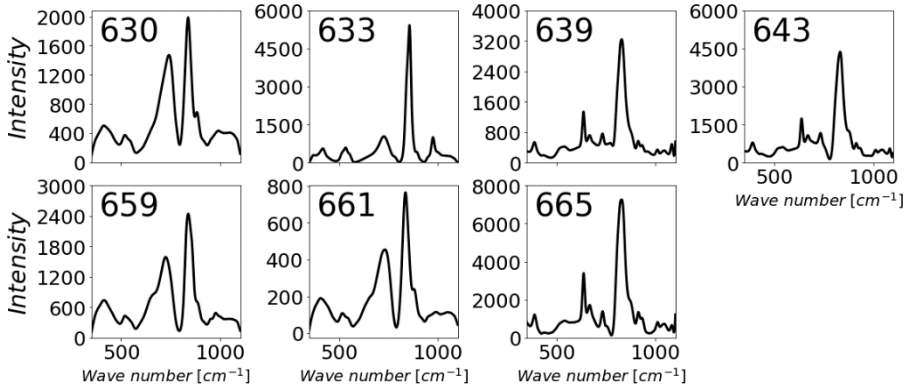

Figure 3. Average Raman spectra for the studied samples.

The Raman intensity is mainly affected by the following factors: 1) the light source intensity; 2) the wavelength of the source; 3) the concentration of the sample or the number of molecules being scattered and; 4) the scattering properties of the sample. The first two factors are constant for all clinkers, while the latter two vary even within a single experiment. One has to consider that the total scattering intensity could vary from point to point depending on the local sample morphology and its orientation towards the detector. The determination of the mineral phase distribution can then be seen as a biased sampling without replacement experiment for a multivariate hypergeometric distribution. In this case the discrete variable consists of one out of five mineral phases (two morphologies of C_3A must be considered separately) for each of the point measurements. Although the scans were taken sequentially, each point scan is part of an a priori determined geometric grid, making the individual phase detections independent of each other.

The bias was incorporated by assuming that the success rate of detecting a particular phase has a certain weight, which can be either larger or smaller than 1. This scenario complies with Fisher's non-central hypergeometric distribution after the total number of evaluated point scans is known. Therefore, the share of each phase in the

total reflected intensity per point measurement was considered. Accordingly, all these shares per sample were linearly scaled until the number of successes matched a theoretically unbiased hypergeometric distribution based on the bulk X-ray diffraction (XRD) analysis compositions provided by the manufacturer (see table 1). A success was defined as a relative intensity share larger than 0.85.

3. Model Formulation.

As seen in figure 4, the population balance framework is at the centre of the model suggested here. This framework is ideally suited to model how a changing size distribution determines the rheological state of a cement paste. However, it has also been found that parameters such as the aggregation efficiency play a vast role in the model's output. These parameters are in turn determined by the interactions of molecular origin that occur among close granules. While it is possible to obtain reasonable values via fitting, this exercise can obfuscate relevant information and it limits the generality of the model (Gallo-Molina et al., 2020). Accordingly, it is believed that directly including information regarding the mentioned interactions is a necessity for the construction of a truly mechanistic model of cement rheology. However, it has been observed that the continuous mathematical approximations that are often used to obtain this kind of information in colloidal systems (e.g., the well-known DLVO theory) have severe limitations in their applicability for the system at hand. This is caused by fact that it is not clear whether these models' assumptions are valid in cement suspensions and due to the unavailability of their required parameters (Flatt & Bowen, 2003; Lomboy et al., 2011).

For these reasons, in this study it was decided to use the information derived from the MD simulations described in a previous publication (Gallo-Molina et al., 2021) to construct a more general model of fresh cement paste rheology. Since the employed force field parameters were obtained from quantum mechanical calculations and atomistic experimental methods (Cygan et al., 2004; Freitas et al., 2015; Honorio et al., 2020; Madura & Jorgensen, 1986; Wu et al., 2006), this approach sidesteps the hurdles encountered when one tries to obtain the necessary parameters for a continuous model. Moreover, the use of MD allows for the explicit consideration of different molecular compositions, which can be useful to assess the effect of different product formulations. Here, the challenge lies in making the connection between the nanoscale information given by MD and the mesoscale, as modelled by PBM.

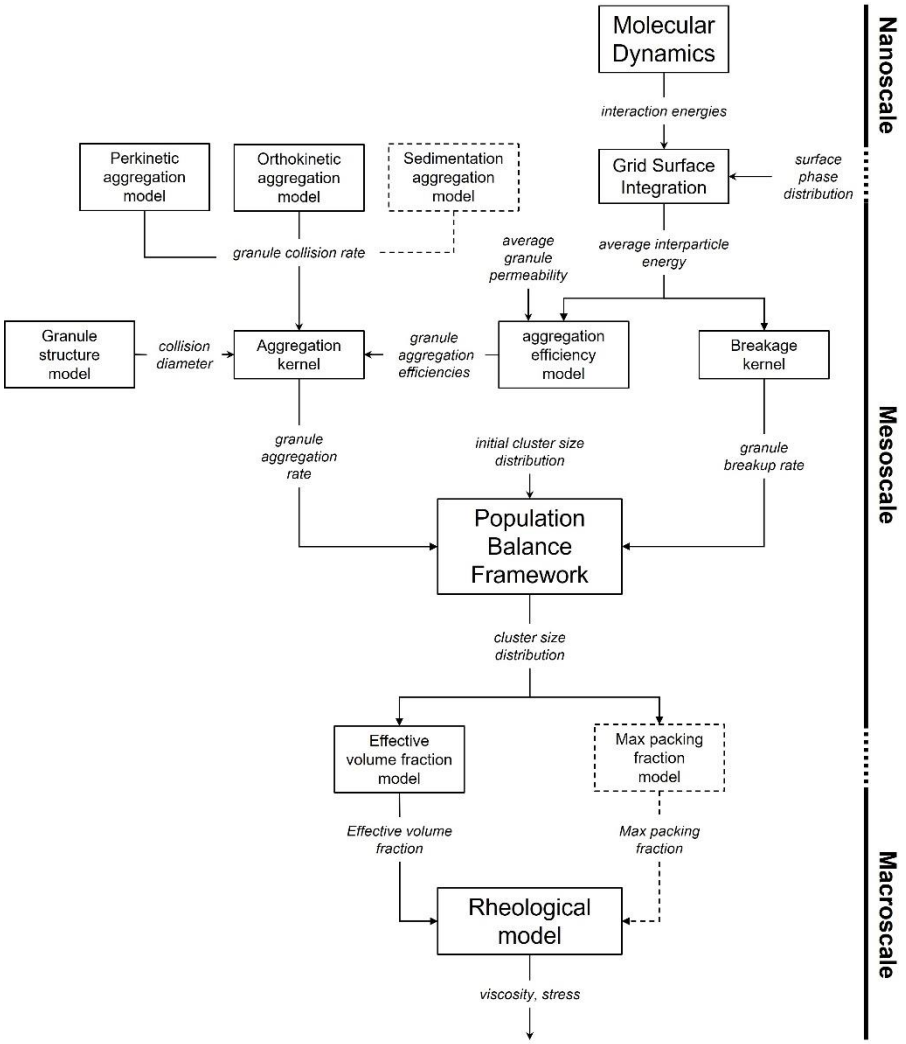

Figure 4. Schematic representation of the proposed model structure. Boxes represent model modules, while italic phrases are calculated quantities. Dashed lines correspond to additional elements that could be considered depending on the target application. The two main inputs are the initial size distribution of the paste and the phase surface distribution in the granules.

The initial step in the construction of the model is the population balance equation, which in a general form reads (Ramkrishna, 2000) :

$$\frac{\partial n}{\partial t} + \nabla_{\tilde{x}} \cdot (v_{\tilde{x}} f_1) + \nabla_{\tilde{r}} \cdot (v_{\tilde{r}} f_1) = \hat{h} \quad (1)$$

The first term on the left-hand side of equation 1 is an accumulation term of the particle number density, *n*. The second and third term quantifies the change in number density due to advection in external and internal coordinates, respectively. The external coordinate set, $\tilde{r}$, corresponds to physical space, while the internal set, $\tilde{x}$,

corresponds to the tracked property or group of properties (e.g., particle size). The term on the right-hand side of equation 1 represents the net generation of aggregates due to discrete processes.

If the system can be assumed to be well mixed, the previous equation can be rewritten (Kumar et al., 2008; Ramkrishna, 2000; Yeoh et al., 2014):

$$\frac{\partial n}{\partial t} = \frac{1}{2}\int_0^x \beta(x-\epsilon,\epsilon,t)n(x-\epsilon,t)n(\epsilon,t)d\epsilon - \int_0^\infty \beta(x,\epsilon,t)n(\epsilon,t)d\epsilon + \int_0^\infty b(x,\epsilon)S(\epsilon)n(\epsilon,t)d\epsilon - S(x)n(x,t) \quad (2)$$

In the previous expression, the first two terms on the right-hand correspond respectively to the birth and death of clusters due to aggregation. The last two terms represent respectively the birth and death of clusters caused by breakage. The aggregation kernel, β, represents the rate at which aggregation events between particles of different size occur, while the selection function, S, indicates the rate at which clusters of size ϵ are selected to break. The breakage function, b, corresponds to a probability density function for the formation of clusters of size x after aggregates of size ϵ have broken up.

Equation 2 was numerically solved using the Cell Average Technique (CAT), which has been extensively described elsewhere (Gallo-Molina et al., 2020; Kumar et al., 2006, 2008). In this approximation, the continuous PSD is discretized into a finite number of size intervals (cells). As a result, equation 2 transforms into a set of Ordinary Differential Equations (ODE); one per cell. Each one of these equations quantifies the number concentration of particles within a given size interval as a function of the net rate of birth and death of particles due to aggregation and breakage, which in turn require the previously alluded aggregation kernel, selection function and breakage function. The suitability of CAT within the context of the application at hand has been demonstrated in a recent publication (Gallo-Molina et al., 2020).

The size dependent aggregation kernel can be further expressed as the product of a collision rate, θ, and the probability that a given collision results in actual aggregation of the particles. The latter variable is captured by the aggregation efficiency term, λ, in equation 3.

$$\beta_{j,k} = \lambda_{j,k}\theta_{j,k} \quad (3)$$

where j and k refer to the sizes of the interacting particles.

The collision frequency mechanism is almost exclusively dependant on the size range of the involved aggregates. In this work, the shear-induced orthokinetic mechanism was assumed to be the dominant one due to the typical

size of cement particles. In this regime, relative movements among particles are induced by a non-uniform velocity field, while in perikinetic agglomeration, these movements are produced by the thermal, Brownian motion of the particles. No sedimentation terms were added for the reason that settling velocities in highly concentrated systems are not expected to be large enough to promote significant agglomeration in the small samples used during controlled rheological experiments (Ha & Liu, 2008; Han & Lawler, 1992; R. Jeldres et al., 2018; R. I. Jeldres et al., 2015; Wheeler & Chatterji, 1972). Equation 3 can therefore be further elaborated as follows:

$$\beta_{j,k} = \lambda_{j,k}^{O}\left[\frac{4}{3}\dot{\gamma}\left(r_j + r_k\right)^3\right] + \lambda_{j,k}^{P}\left[\frac{2k_bT}{3\mu}\frac{\left(r_j + r_k\right)^2}{r_j r_k}\right] \quad (4)$$

where $\dot{\gamma}$ is the shear rate, r is the radius of colliding aggregates of size j and k, k_b is the Boltzmann constant, T is the temperature and μ is the fluid viscosity.

The first term on the right-hand size of equation 4 gives the rate of aggregation events due to shear-induced agglomeration, while the second one can be used to compute Brownian agglomeration events (Smoluchowski, 1917). In turn, it is well-known that the eventual outcome of each event is dependent on the interaction forces between the particles. However, the specific mechanism changes with the size scale. For submicron sized elements, hydrodynamic effects are negligible, while the relative magnitude of the particle's thermal energy compared to that of interactive forces determines whether aggregation can take place. Conversely, for larger particles Brownian motion stops being relevant, while hydrodynamics starts playing a significant role in combating or supplementing interactive forces (Agarwal, 2002; R. I. Jeldres et al., 2015; Vanni, 2000; Vanni & Baldi, 2002). For this reason, equation 4 contemplates two aggregation efficiency terms: one for the orthokinetic regime ($\lambda_{j,k}^{O}$) and the other for the perikinetic mechanism ($\lambda_{j,k}^{P}$). As it will become apparent in subsequent subsections, both terms require knowledge of the system's molecular interactions.

In order to account for the lack of sphericity of cement aggregates, a characteristic mass fractal dimension (Barthelmes et al., 2003; Flesch et al., 1999; Mandelbrot, 1982) was used here. This is of importance for rheological predictions since the irregularity of the aggregates affect the way they interact with the fluid medium and themselves. Furthermore, this phenomenon allows for the entrapment of water in interstitial spaces. Consequently, an effective volume fraction was used as the bridge between the meso and macroscales:

$$\phi_{eff} = \phi\left(\frac{\bar{r}_{agg}}{\bar{r}_p}\right)^{3-D_f} \quad (5)$$

In equation 5, ϕ is the nominal solids volume fraction of the suspension, which can be readily be calculated from the water to cement ratio; a more commonly used metric in the industry. Moreover, $\bar{r}_{agg}$ is the volume-weighted mean particle radius obtained at any given time from PBM calculations, and D_f is the fractal dimension. This variable was treated here as a fitted parameter, but it can potentially be measured and/or described in a more sophisticated manner, such as the one proposed by Selomulya et al. (2002).

Finally, rheological observables can be accessed by, for example, applying the Quemada constitutive equation (equation 6). However, as suggested by figure 4, other approaches such as the calculation of maximum packing fraction from the PSD could be implemented if needed.

$$\mu = \mu_0 \left(1 - \frac{\phi_{eff}}{\phi_{max}}\right)^{-2} \tag{6}$$

Here, μ_0 is the viscosity of the suspending medium (water) and ϕ_{max} is the maximum packing fraction. In this work, the latter variable was assumed to adopt a value of 70%, which is an average for cement suspensions (de La Rosa et al., 2021; Struble & Sun, 1995). If required, the maximum packing fraction could be calculated by other means or treated as a fitted parameter.

3.1. Orthokinetic aggregation efficiency.

The expression in square brackets in the first term on the right-hand size of equation 4 was derived assuming that particles follow a rectilinear trajectory, which implies that no interaction forces are present, and the flow field is not perturbed. In actuality, when they are in close proximity, an approaching particle's trajectory will bend and, depending on the forces in play, aggregation may not occur. This discrepancy between the ideal and real scenarios can be quantified with an efficiency term. Unfortunately, currently there is not an adequate single mechanistic expression capable of quantifying said efficiency without the need for one or more empirical parameters that must be fitted.

Considering this, trajectory analysis was implemented in order to deduce these efficiencies under different circumstances. As seen in figure 5, if a particle of a given size is fixed at the centre of a coordinate system, the relative trajectory of a second particle under a known set of process and environmental conditions can be obtained if Stokes flow is assumed. This simplification is warranted given the small length scales and shear rates involved and it allows for a decomposition of the overall particle velocity into the sum of the velocity caused by the fluid flow and that induced by molecular interactive forces (Adler, 1981; van de Ven & Mason, 1976). Consequently,

for the reference system illustrated by figure 5, the position of a particle *j* relative to a particle *k* is given by equations 5-7 (Vanni & Baldi, 2002).

$$\frac{d\hat{r}}{dr} = \dot{\gamma}(1 - A)\sin^2\theta\sin\phi\cos\phi + \frac{C}{6\pi\mu a_k}F^T\left(\hat{r}, r_j, r_k\right) \tag{5}$$

$$\frac{d\theta}{dt} = \dot{\gamma}(1 - B)\sin\theta\cos\theta\sin\phi\cos\phi \tag{6}$$

$$\frac{d\phi}{dt} = \dot{\gamma}\left(\cos^2\phi - \frac{B}{2}\cos 2\phi\right) \tag{7}$$

In the above equations, $\hat{r}$, θ and ϕ are the radial, azimuthal and polar positions of particle *j*, respectively. *A* and *B* are hydrodynamic functions which emerge when a description of the particle's relative velocity due to fluid flow is obtained. Analogously, *C* emerges when the relative velocity induced by the radially acting interparticle force, F^T , is taken into account (Bäbler et al., 2006). This colloidal force was derived from MD calculations as described in Section 3.3.

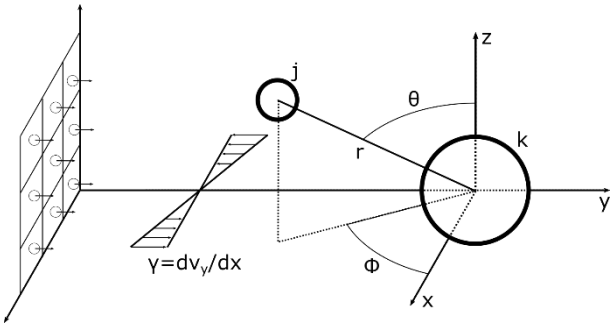

Figure 5. Reference system used to calculate orthokinetic aggregation efficiencies. A particle *k* is located at the origin, while a particle *j* approaches. Velocity in the y-direction changes only with respect to x. A grid in the x-z plane was generated far enough from the centre and a particle *j* was released from the centre of each cell. The trajectory of each released particle can be analysed to deduce a collision cross section, which is the used to estimate the aggregation efficiency.

The aforementioned hydrodynamic functions were developed by Bäbler et al. (2006) using physical arguments and are described by equations 8-10. These functions take into consideration that the perturbation of the flow is dependent on the permeability of the particles, which is an important consideration given that cement agglomerates are known to be porous.

$$A = \frac{5}{2}\frac{Q_{2,k}r_k^3 + Q_{2,j}r_j^3}{\hat{r}^3} - \frac{\frac{3}{2}\left(Q_{1,k}r_k^5 + Q_{1,j}r_j^5\right) + \frac{5}{2}r_k^2 r_j^2\left(r_k Q_{2,k}S_j + r_j Q_{2,j}S_k\right)}{\hat{r}^5} + \frac{25a_k^3 Q_{2,k}r_j^3 Q_{2,j}}{\hat{r}^6} + \frac{25}{3}\frac{r_k^3 Q_{2,k}r_j^3 Q_{2,j}\left(r_k^2 S_k + r_j^2 S_j\right)}{\hat{r}^8} \quad (8)$$

$$B = \frac{Q_{1,k}r_k^5 + Q_{1,j}r_j^5 + \frac{5}{3}r_k^2 r_j^2\left(r_k Q_{2,k}S_j + r_j Q_{2,j}S_k\right)}{\hat{r}^5} + \frac{25}{3}\frac{r_k^3 Q_{2,k}r_j^3 Q_{2,j}\left(r_k^2 S_k + r_j^2 S_j\right)}{\hat{r}^8} \quad (9)$$

$$C = \frac{r_j C_{kk} + r_k C_{jj}}{r_j + r_k} - \frac{4r_j r_k C_{jk}}{\left(r_j + r_k\right)^2} \quad (10)$$

In the previous expressions, Q_1, Q_2 and S are shielding functions that depend only on a shielding ratio, ξ, and account for the porous structure of the particle. In turn, C_{kk}, C_{jk} and C_{jj} are mobility functions that introduce the effect of velocity disturbances along the centres of the particles. They depend on the shielding ratio and the radii of the particles. These functions are derived and presented in the original reference (Bäbler et al., 2006).

The shielding ratio, ξ, is the inverse of the dimensionless permeability as follows:

$$\xi_k = \frac{r_k}{\sqrt{\kappa}} \quad (11)$$

where κ is the permeability of the particles. This latter parameter can be measured, fitted or estimated in function of the particle's porosity, as described in the literature (Li & Logan, 2001; Yu & Cheng, 2002; Yu & Li, 2001; Yu & Liu, 2004).

The system of ODE described by equations 5-7 can be solved for different starting positions of particle *j*. If all these positions are located on a plane perpendicular to the flow, far away from particle *k*, and subdivided into a grid, a collision cross-section can be constructed after determining the eventual fate (aggregation or no aggregation) for each starting position. This was accomplished by using the conditions for primary and secondary aggregation shown by Vanni & Baldi (2002). Considering that interactive forces only act on the radial direction, this grid was restricted to only one of the quadrants in the x-z axis. The length of each side of the grid was fixed as 1.5 times the sum of the interacting particles radii and a minimum of 30 x 30 cells was used, with additional refinements as needed. Each trajectory can be calculated in parallel, which allows for a full integration with the overall model. However, if one or more of the operating conditions (e.g., shear rate) are known in advance, a

response surface can be pre-computed and used subsequently by the rest of the model or to construct a surrogate expression. Subsequently, the shear and composition dependent orthokinetic aggregation efficiency was calculated by comparing the actual and ideal collision cross-section areas, as illustrated by equation 12.

$$\lambda_{j,k}^{O} = \frac{3}{2}\frac{1}{\left(r_j + r_k\right)^3}\int_0^{z_\infty}[x(z)]^2 dz \tag{12}$$

In the above expression, the integrand corresponds to the real collision cross-section within the coordinate system given in figure 6.

3.2. Perikinetic aggregation efficiency and breakage kernel.

Although they are not overall predominant in cement suspensions, Brownian induced agglomeration events start having a noticeable role in the finer fractions of the PSD and are significantly more important in other constituents of concrete mixtures such as silica fume. Therefore, and for the sake of completeness, a perikinetic aggregation rate was included in the model. Unlike the orthokinetic mechanism, in perikinetic aggregation particles acquire a relative trajectory towards each other due to their random thermal energy. In this case, the interaction forces between the particles also determine whether a collision results in aggregation, which implies the necessity of a second efficiency term that corrects for the ideal scenario painted for the derivation of the collision rate expression in equation 4. In this work the inverse Fuchs stability ratio was used to obtain said efficiency. As presented in equation 13, this ratio compares the rate of agglomeration in the absence of molecular interactions with that occurring under realistic conditions (Fuchs, 1934; Honig et al., 1971; Runkana et al., 2005).

$$\lambda_{j,k}^{p\ -1} = \left(r_j + r_k\right)\int_{r_j+r_k}^{\infty}\frac{\exp\left(\frac{\bar{r}_{j,k}sF(s)}{k_bT}\right)}{s^2}ds \tag{13}$$

Where F is the normalized interaction force (derived from MD calculations, as described in section 3.3.) and $\bar{r}_{j,k}$ is defined as follows.

$$\bar{r}_{j,k} = \frac{2r_j r_k}{r_j + r_k} \tag{14}$$

The selection rate for breakage was calculated using equation 15 which, as discussed by Puisto et al. (2012), compare the hydrodynamic stress that tends to break the aggregates up with the forces that hold them together.

$$S_k = \dot{\gamma} \exp\left(-\frac{2F_c}{5\pi r_k^2 \mu \dot{\gamma}}\right) \quad (15)$$

The effective bound force, F_c, was approximated using the attractive minimum of the colloidal forces derived from MD.

Considering that currently it is not clear what is the exact mechanism of breakage in cement aggregates, a binary breakage function was assumed in this case. More details are offered in a previous work (Gallo-Molina et al., 2020).

3.3. Estimation of colloidal interactions via Molecular Dynamics.

As discussed above, the estimation of the colloidal forces acting among granules in close proximity was done with the assistance of MD calculations, for the reason that this technique allows for a significantly higher level of detail in the predictions of said forces. A comprehensive simulation study was performed with the MD package DL POLY 2.20 (Todorov et al., 2006). In this study, simulation boxes containing two crystalline slabs of the same or different composition (considering all the possible permutations of the phases presented in figure 1) were generated. These slabs were separated by an aqueous solution of calcium hydroxide in order to mimic the real environment of a typical cement suspension. The length of the sides of the slabs was approximately 5 nm and the separation distance was varied from 0.5 to 12 nm. Temperature and pressure were fixed as 300 K and 1 atm, respectively. A general force field with fixed partial charges was used to predict atomic interactions and the colloidal forces were obtained from the atomic trajectories after an adequate equilibration time had elapsed. The total simulation time was at least 1.5 ns and the mass and volume of the simulations boxes were kept constant. For the sake of illustration, figure 6 shows the different normalized force-distance curves obtained from these calculations. Each line corresponds to different combination of clinker compositions and, as it can be appreciated, significant deviations were predicted. As could be expected, this implies that the product formulation has an important influence in the aggregation and breakage dynamics. Additional details and discussion are presented elsewhere (Gallo-Molina et al., 2021).

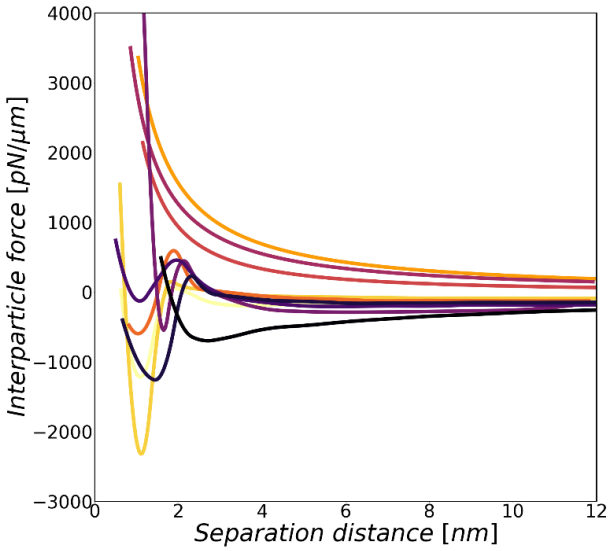

Figure 6. Interaction force between different pairs of cement clinker phases as a function of separation distance. Negative values represent attractive forces.

Each of the obtained force-distance curves offer an accurate representation of the interactions among the two phases for which they were obtained, but individually they cannot offer a representative picture of the situation in a real system due to the compositional heterogeneity in the typical clinker granule and the differences in size scales. For this reason, a connection must be established between the clinker formulation and the obtained MD results. This was achieved by an implementation of the Grid Surface Integration (GSI) technique, which has been successfully employed in the past to describe the interactions between chemically heterogeneous particles (Bendersky & Davis, 2011; Duffadar & Davis, 2007, 2008; Ma et al., 2011). In this method, the particles are discretized in a grid (in which each grid element has its own composition) and then the pair-wise interactions between cells are calculated and ultimately summed in order to obtain the overall interaction between the two bodies.

This approach is shown in figure 7. There, each cell colour represents one of the phase compositions considered here (e.g., C_3S, C_2S, etc.). Since the radius of a typical clinker particle is substantially larger than the separation distances relevant for colloidal interactions in cement pastes (Roussel et al., 2010), a representative area of each interacting granule can be assumed to be a planar surface. Therefore, the whole system becomes a collection of the scenarios individually simulated with MD (figure 7a). As shown in figure 7b, the interactions due to each of the cells (dS) in one surface can be integrated over the whole plane in order to obtain the force acting on a grid element (dA) in the opposite particle, as described by equation 16.

$$dF = \sum_{surface\ 1} P(h)(e_1 \cdot e_z)dS \tag{16}$$

Where *P(h)* is the force between cells when the distance between the surfaces is *h*; e_1 is the unit vector that gives the direction between cells; and e_z is the unit vector normal to the *z*-direction.

A second integration can then be performed in order to calculate the total interaction between the surfaces:

$$F = \sum_{surface\ 2} dF \tag{17}$$

The selection of the grid composition was done considering that the percentual content of each phase on the surfaces can differ significantly from the nominal formulation of the clinker (Erdoğan, 2013; Mohamed et al., 2014; Schmid & Dariz, 2019). For this reason, the surface distributions derived from Raman spectroscopy (see section 2) were used as an input and effective distributions were generated on sufficiently large grids in which the background phase was assumed to be C_3S. The remaining phases were emplaced in such a way that the (randomly generated) clusters they formed had a total surface area equal to the experimentally derived one and their spread was analogous to what was observed. In order to obtain a final, representative picture of the distance dependent forces between particles, this exercise was repeated a large number of times and the Monte Carlo method was implemented to calculate the average force-distance curve of the system. This curve was subsequently used to inform the aggregation and breakage kernels and discussed in sections 3.1 and 3.2.

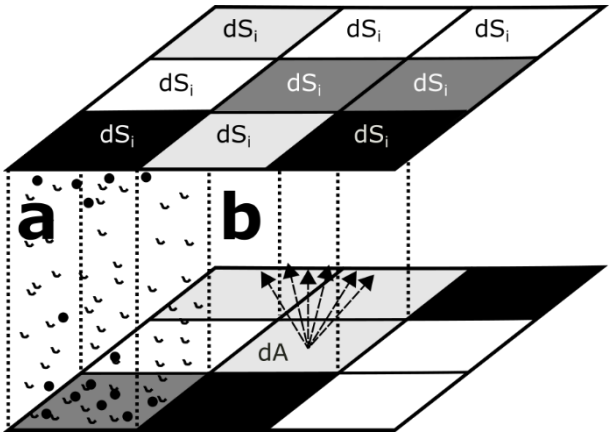

Figure 7. Schematic representation of the methodology used to obtain the average interaction between granules. A representative area of each particle was taken to be planar, and it was divided in a number of cells, each of which was assigned a composition (shade of grey). Each possible combination was simulated with MD (a) and its specific interaction was derived. The GSI technique was subsequently used to calculate the overall interaction (b).

4. Results and Discussion.

The viscosity evolution over time is presented in figure 8a, where the shaded areas correspond to the 95% significance intervals based on the three experimental repetitions. In all cases viscosity increases over time, but the extent varies according to the value reached at the end of the pre-shear. As seen on panel a), a large degree of overlapping was observed along the rheological behaviour of all the analysed cements. This was to be expected, since the initial size distributions of all the samples as well as the treatment they were subjected to prior to experimentation were similar. Although this information could not be directly observed, it is believed that the evolution of the PSD was generally comparable in all cases.

It is nevertheless possible to assert that significant differences in rheology were observed among some samples. As seen on figure 8b, a subset of the explored cements was selected considering that their 95% confidence intervals do not overlap, which implies that they indeed exhibit significantly different behaviours. It can be observed how the viscosity for paste 633 is generally higher than for paste 665, which is again higher compared to paste 630. With the pastes having very similar initial size distributions, the difference in rheology needs to be sought in the surface composition of the clinker phases. From the above rheological observations, one could conclude that the surface activity in paste 633 is higher than for paste 665, which is in turn higher than for paste 630.

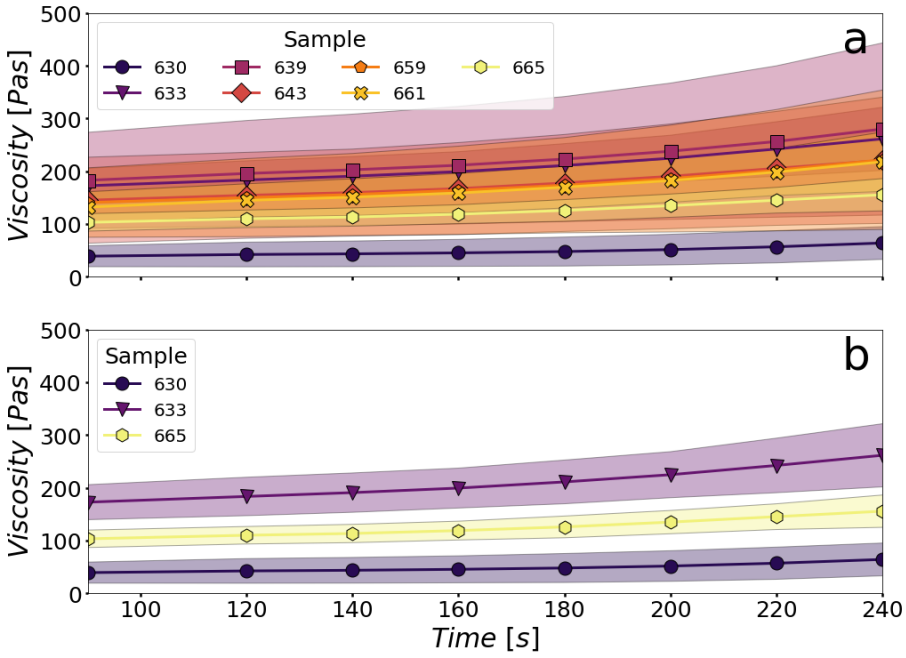

Figure 8. Viscosity vs time measurements for all the studied samples (a) and the selected subset (b). Shaded areas correspond to the 95% confidence intervals.

The distribution of the several phases present on the surfaces of the granules of the three selected clinkers was derived from Raman spectra and is shown in figure 9. There, each pixel corresponds to one of the measurement locations and the colour denotes the detected composition. It can be seen that in all three cases, C_2S (blue), C_3A, (yellow, red) and C_4AF (green) regions occur over the backdrop of the dominant C_3S (brown) phase. Furthermore, and as illustrated by table 1, significant differences were observed between the bulk composition of the clinker (measured by the manufactured using XRD analysis) and the superficial availabilities of the main phases, which is what actually impacts the aggregation dynamics of the paste.

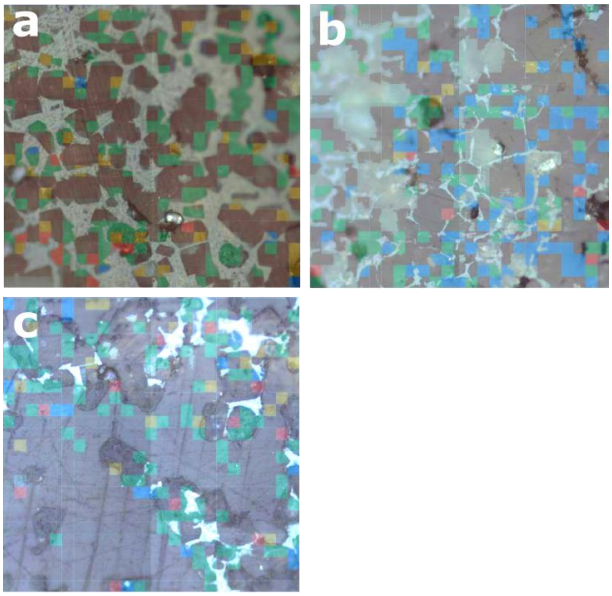

Figure 9. Phase surface distributions for three selected samples. Brown: C_3S; blue: C_2S; yellow: C_3Aa; red: C_3Ab; green:C_4AF. a) 630, b) 633, c) 665.

Table 1. Bulk (surface) phase compositions of the selected samples.

Sample	**630**	**633**	**665**
C_3S [%]	73.3 (65.7)	65.6 (51.7)	73.6 (77.6)
C_2S [%]	2.1 (1.2)	9.0 (35.1)	3.1 (2.6)
C_3A [%]	5.8 (10.0)	6.3 (2.2)	4.4 (4.6)
C_4AF [%]	17.4 (23.2)	16.0 (11.0)	16.0 (15.3)

It was observed that the clinker 630 is particularly rich in C_3A and C_4AF and phases, followed by sample 665. Sample 633 exhibited the least amount of these compounds on the surface but contains a disproportionate quantity of C_2S. It seems that a higher presence of C_3A and C_4AF is related in this instance with smaller overall viscosities, which is likely connected to large repulsive interactions generated by the higher concentrations of these compounds. In the case of clinker 630, the particularly high amount of C_3A and C_4AF can also potentially be linked with the particle segregation that is believed to have occurred during and after rheological experiments, as evidenced by the virtually flat viscosity curve and its relatively small magnitudes. It is expected that these

differences in composition play a key role in the determination of the interparticle interactions that drive aggregation and breakage dynamics during the shear experiments. As the studied pastes are highly concentrated suspensions, these dynamics should in turn largely determine the rheological response.

In order to assess the capacity of the model proposed in section 3 to reproduce the observed flow behaviours, the pipeline illustrated by figure 4 was followed. As described before, the results obtained from molecular dynamics can be used to generate an estimation of the overall interactive forces among the granules in a given system. This can then be used to calculate aggregation and breakage dynamics, which play a very important role in the evolution of the particle size distribution and, eventually, rheology. The phase surface distributions obtained from Raman spectroscopy were used as an input. These results represent a good test bench, since the clinker samples showed significantly different rheological behaviours even though their initial size distribution were close to identical.

Figure 10 shows the computed interaction forces for the studied powders. For each sample, 1000 GSI grid pairs were populated with random clusters that had total surface areas and spreads equivalent to the corresponding experimental value. The planes were given a side length of one micron for the reason that this is the order of magnitude of the zone of electrostatic influence in cementitious systems (Flatt, 1999). As illustrated by the figure, significant departures from the force profile of hypothetical pure C_3S granules were observed. The differences in the shape of curves are caused by the introduction of extra chemical compounds, while the changes in magnitude can be attributed to the reinforcing or dampening contributions (which depend on both distance and sample) that a given unit area of surface is subjected to due to nearby heterogeneities. As concluded by Nachbaur et al. (1998), this phenomenon is expected in cement pastes. It is one of the reasons for their strong coagulating behaviour and it causes the predicted lengthening of the tails of the profiles.

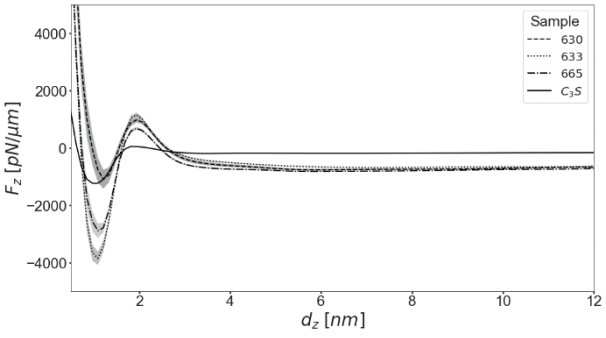

Figure 10. Computed average force-distance curves for different samples and a hypothetical pure C_3S system. Shaded areas correspond to the 95% confidence intervals. Negative values represent attractive forces.

Important differences were predicted among clinkers as well. For instance, the attractive minimum of sample 633 (dotted line) is considerably smaller than that of clinker 630 (dashed line). Additionally, small shifts in the location of the minima were observed, while the repulsive maxima and the long-range force decay were predicted to be affected as well. In the case of the former sample, the existence of large quantities of C_2S can be ascribed as a main reason for its deep attractive well, while the opposite effect observed in the latter case seems to be connected to the presence of large quantities of C_3A and C_4AF (for more discussion on the chemical origin of these effects see the work of Gallo-Molina et al. (2021) and references within).

The measured size distribution of each clinker was used as the model initial condition, while the calculated force profiles were implemented as the basis for the computation of efficiencies and bound forces as described in previous sections. Since the hydraulic permeabilities of the clinkers and their fractal dimensions could not be measured, a partial calibration was performed using the flow curve of sample 665. As a result, the estimated values of the fractal dimension and permeability were 2.77 and 2.89E-13 m^2, respectively. These values were kept constant in all cases.

Figure 11 demonstrates that the model is indeed capable of predicting the three different flow curves measured for the studied samples. The fit is good for clinker 665, since the data was used for the aforementioned calibration. However, it can be seen that in the remaining two cases, the model is able to predict values within the uncertainty intervals of the data, which suggests that the approach proposed in this work can be valuable as a way of describing the rheological evolution of early cement pastes. Nevertheless, it must be stressed that further experiments are required to further validate the model. In this case, it is believed that the fitting of the two alluded parameters allows it to compensate for non-considered phenomena such as the presence of early hydration products. A complete calibration (in the presence of a richer data set) could be considered in the future to build surrogate expressions that account for these weaknesses.

Perhaps more interestingly, figure 12 illustrates the underlying evolution of the particle size distribution of each sample as predicted by the model. Since this information could not be directly measured, it is not possible to assess the accuracy of the absolute values. However, it can be argued that the relative differences among the distributions should be in line with reality. In all three cases the general evolution is similar, as would be expected. A shift of the distribution to the left (dotted line to dashed line) indicates that the executed pre-shear broke down a significant fraction of the aggregates (especially the larger, more unstable ones) till an equilibrium was reached. The smallest aggregates presented certain amounts of agglomeration due to the fact that in that region the

hydrodynamic effect of shear is less important, while attractive forces are more relevant (Vanni & Baldi, 2002). Subsequently, the shift to the right observed in the final states (continuous lines) shows that the model can adequately predict the restructuring process that occurs during the stepdown protocol. The fact that the particles do not tend to return to their initial state leads to thixotropic characteristics. These dynamics are consistent with previous observations made with focused beam reflectance probes under similar conditions (Eslami Pirharati et al., 2020; Ferron et al., 2013; Thiedeitz et al., 2020).

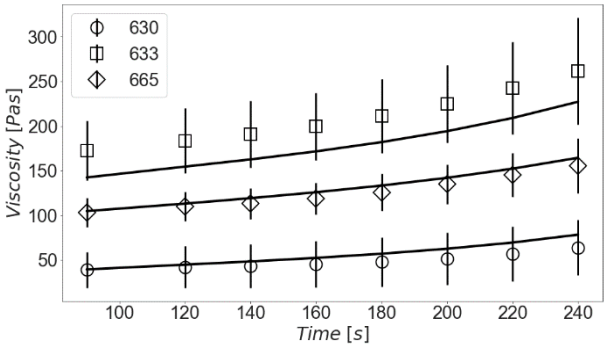

Figure 11. Comparison between model prediction (continuous lines) and experimental measurements for three clinker samples. The vertical lines denote the 95% confidence intervals.

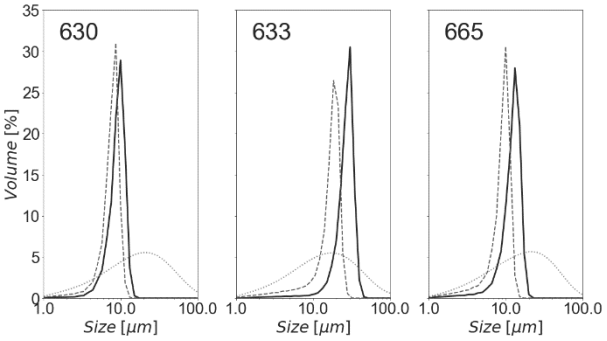

Figure 12. Evolution of the PSD for the simulated shear test and studied clinker samples. The dotted lines represent the dry distributions, the dashed lines denote the distributions at 120 s, and the continuous line corresponds to the final state at 240 s.

It can be seen that particles broke up in a much higher degree in sample 630 and that the predicted restructuring was weaker as evidenced by the smaller shift of the peak to the right. This situation arises from the shallow attractive minimum predicted for the system, which indicates fragile clusters that are also in the presence of relatively strong repulsive forces. Since the estimated flow curve seems to overshoot, it is possible that an overestimation of the restructuring process is being made due to missing information in the model. In any case,

the intermediate and final PSDs seem to be consistent with the experimentally observed particle segregation in sample 630.

Conversely, cement 633 exhibited the sharpest reaggregation dynamics of all three systems, which results in a higher viscosity both predicted and observed. Once more, this can be attributed to the interactive forces expected among the granules. The considerable attractive forces present between clusters both enhance aggregation and somewhat inhibited the destruction of the agglomerates during the initial phase of the experiment. This last affirmation can also be substantiated if one compares the dashed curves in figure 12 for systems 633 and 665: that of the former has a smaller mean size, which can be attributed to cement 633 being overall more attractive. This makes its clusters more resistant to breakage. Finally, the smaller fractions of all three cements seem to have dynamics favouring aggregation, the strength of which also followed the same patterns.

The model developed here can be seen as a possible way forward in the quest to successfully connect the many phenomena affecting the rheology of cementitious materials. It is believed that the proposed approach is capable of reproducing the major dynamics that determine rheological properties during the early age of a cement paste. However, more work is necessary. For instance, the consideration of the influence of superplasticisers -which reduce overall attractive interparticle forces (Thiedeitz et al., 2020) would increase the practical applicability of the framework. Moreover, the reaction of C_3A with sulphate to produce ettringite was not explicitly considered. While the influence of this phenomenon on the dynamics of the PSD should be secondary at first (Holzer et al., 2007; Thiedeitz et al., 2020; Zingg et al., 2008), it is bound to affect the overall interactive forces of the system. This problem could be alleviated in a relatively straightforward fashion within the presented modelling framework by including MD calculations for the mentioned reaction product. Consequently, a kinetic model for the hydration of C_3A based on calorimetric information (see, for example, the work of Ukrainczyk (2010)) or even an ad-hoc empirical expression could be used to estimate the amount of ettringite present in a given system. This could then be used to modify the estimated average force-distance curve that would be subsequently employed for PBM calculations. In a similar manner, the gradual appearance of other hydration products could be considered by the model.

5. Conclusions.

In this work, a scaling up method of the information obtained from molecular dynamics simulations is suggested. By using experimental measurements of the distribution of the different phases present in cement granules, it was possible to generate a statistically equivalent picture of said distribution. Subsequently, grid surface integration

was implemented in order to obtain the expected mean force-distance curve of a given system from the several one-on-one MD simulation results and as a function of the aforementioned measured superficial phase distributions. This information was then used to parametrize aggregation and breakage kernels within the context of a population balance model.

While the collision frequency term of said kernel was kept as the classic Smoluchowski coagulation equation, a powerful methodology to calculate the aggregation efficiency term was introduced. This methodology is based on trajectory analysis and it uses the computed interaction forces of a given sample to estimate the probabilities of aggregation under specific hydrodynamic conditions. This, in conjunction with the developed PBM model constitutes a multiscale framework geared towards the prediction of the flow behaviour of early cement pastes.

The proposed model was tested with the experimental information and its performance was shown to be satisfactory. By using the measured size and surface phase distributions of each of the studied samples, the model was able to adequately predict the differences in observed flow curves. The underlying dynamics of the particle size distributions were also observed to be in line with their expected behaviour. However, more testing against experiments is warranted. Further refinements in the shape of an explicit consideration of early hydration reactions or the inclusion of the influence of superplasticisers or other admixtures were identified as ways to improve the capabilities of the model. Regardless, it can be concluded that the suggested modelling methodology constitutes a promising alternative to start solving the complex puzzle that is cement rheology.

This modelling method thus offers interesting possibilities for its application in an industrial setting. For instance, the explicit inclusion of the clinker composition in the structure of the model opens the door to its utilization in optimisation exercises that would seek to reach an ideal combination of both formulation and powder fineness for a given application (for which a specific rheology would be desired). Moreover, after validation, the model could be used in lieu of, or complementary to traditional empirical tests to obtain a more robust picture of the state of the paste. This could prove invaluable during processes such as transport, pumping and placing.

6. Acknowledgements.

The authors gratefully acknowledge the financial support received from the Research Foundation Flanders through grants G017616N and V431319N.

The assistance of Prof. Peter Vandenabeele and Ms. Sylvia Lycke in collecting and postprocessing the Raman spectra is gratefully acknowledged.

7. Nomenclature.

b	Breakage function (m^3)
D_f	Mass fractal dimension (-)
F	Normalized interparticle force ($N\ m^{-1}$)
F_c	Effective bound force (N)
F^T	Interparticle force (N)
n	Particle number density (m^{-6})
P	Force between GSI cells (N)
r	Particle radius (m)
$\bar{r}_{agg}$	Volume-weighted mean particle radius (m)
S	Selection function (s^{-1})
T	Temperature (K)

Greek Letters

β	Aggregation kernel ($m^3\ s^{-1}$)
$\dot{\gamma}$	Shear rate (s^{-1})
θ	Collision rate ($m^3\ s^{-1}$)
κ	Particle permeability (m^2)
λ	Aggregation efficiency (-)
μ	Fluid viscosity (Pa s)
ξ	Shielding ratio (-)
ϕ	Solids volume fraction (-)
ϕ_{eff}	Effective volume fraction (-)

ϕ_{max} Maximum packing fraction (-)

Subscripts

j,k Particle size classes

Superscripts

O Orthokinetic

P Perikinetic

8. References.

Adler, P. M. (1981). Heterocoagulation in shear flow. *Journal of Colloid and Interface Science*, *83*(1), 106–115. https://doi.org/10.1016/0021-9797(81)90015-1

Agarwal, S. (2002). *Efficiency of Shear-Induced Agglomeration of Particulate Suspensions Subjected to Bridging Flocculation*.

Argyris, D., Tummala, N. R., Striolo, A., & Cole, D. R. (2008). Molecular structure and dynamics in thin water films at the silica and graphite surfaces. *Journal of Physical Chemistry C*, *112*(35), 13587–13599. https://doi.org/10.1021/jp803234a

Bäbler, M. U., Sefcik, J., Morbidelli, M., & Baldyga, J. (2006). Hydrodynamic interactions and orthokinetic collisions of porous aggregates in the Stokes regime. *Physics of Fluids*, *18*(1), 1–18. https://doi.org/10.1063/1.2166125

Barthelmes, G., Pratsinis, S. E., & Buggisch, H. (2003). Particle size distributions and viscosity of suspensions undergoing shear-induced coagulation and fragmentation. *Chemical Engineering Science*, *58*(13), 2893–2902. https://doi.org/10.1016/S0009-2509(03)00133-7

Bendersky, M., & Davis, J. M. (2011). DLVO interaction of colloidal particles with topographically and chemically heterogeneous surfaces. *Journal of Colloid and Interface Science*, *353*(1), 87–97. https://doi.org/10.1016/j.jcis.2010.09.058

Castillo, A., Rozas, F., Martínez, I., & Castellote, M. (2012). Understanding cementitious materials in fresh state: A nano-scale study on the effect of the mixing time. *Journal of Alloys and Compounds*, *536*(SUPPL.1), S569–S574. https://doi.org/10.1016/j.jallcom.2011.12.106

Chidiac, S. E., & Mahmoodzadeh, F. (2009). Plastic viscosity of fresh concrete - A critical review of predictions methods. *Cement and Concrete Composites*, *31*(8), 535–544. https://doi.org/10.1016/j.cemconcomp.2009.02.004

Cygan, R. T., Liang, J. J., & Kalinichev, A. G. (2004). Molecular models of hydroxide, oxyhydroxide, and clay phases and the development of a general force field. *Journal of Physical Chemistry B*, *108*(4), 1255–1266. https://doi.org/10.1021/jp0363287

de La Rosa, Á., Ruiz, G., Castillo, E., & Moreno, R. (2021). Calculation of Dynamic Viscosity in Concentrated Cementitious Suspensions: Probabilistic Approximation and Bayesian Analysis. *Materials*, *14*(8), 1971. https://doi.org/10.3390/ma14081971

Derjaguin, B., & Landau, L. (1993). Theory of the stability of strongly charged lyophobic soils and of the adhesion of strongly charged particles in solutions of electrolytes. *Progress in Surface Science*, *43*(1–4), 30–59. https://doi.org/10.1016/0079-6816(93)90013-L

Duffadar, R. D., & Davis, J. M. (2007). Interaction of micrometer-scale particles with nanotextured surfaces in shear flow. *Journal of Colloid and Interface Science*, *308*(1), 20–29. https://doi.org/10.1016/j.jcis.2006.12.068

Duffadar, R. D., & Davis, J. M. (2008). Dynamic adhesion behavior of micrometer-scale particles flowing over patchy surfaces with nanoscale electrostatic heterogeneity. *Journal of Colloid and Interface Science*, *326*(1), 18–27. https://doi.org/10.1016/j.jcis.2008.07.004

Erdoğan, S. T. (2013). Effect of clinker phase distribution within cement particles on properties of a hydrating cement paste. *Construction and Building Materials*, *38*, 941–949. https://doi.org/10.1016/j.conbuildmat.2012.09.051

Eslami Pirharati, M., Krauss, H.-W., Schilde, C., & Lowke, D. (2020). Effect of Different Shear Rates on Particle Microstructure of Cementitious Materials in a Wide Gap Vane-in-cup Rheometer. *Materials*, *13*(9), 2035. https://doi.org/10.3390/ma13092035

Ferron, R. D., Shah, S., Fuente, E., & Negro, C. (2013). Aggregation and breakage kinetics of fresh cement paste. *Cement and Concrete Research*, *50*, 1–10. https://doi.org/10.1016/j.cemconres.2013.03.002

Flatt, R. J. (1999). *Interparticle Forces and Superplasticizers in Cement Suspensions* [PhD. Thesis, École Polytechnique Fédérale de Lausanne]. https://doi.org/10.5075/epfl-thesis-2040

Flatt, R. J. (2004a). Dispersion forces in cement suspensions. *Cement and Concrete Research*, *34*(3), 399–408. https://doi.org/10.1016/j.cemconres.2003.08.019

Flatt, R. J. (2004b). Towards a prediction of superplasticized concrete rheology. *Materials and Structures/Materiaux et Constructions*, *37*(5), 289–300. https://doi.org/https://doi.org/10.1007/BF02481674

Flatt, R. J., & Bowen, P. (2003). Electrostatic repulsion between particles in cement suspensions: Domain of validity of linearized Poisson-Boltzmann equation for nonideal electrolytes. *Cement and Concrete Research*, *33*(6), 781–791. https://doi.org/10.1016/S0008-8846(02)01059-1

Flatt, R. J., & Bowen, P. (2007). Yield stress of multimodal powder suspensions: An extension of the YODEL (yield stress mODEL). *Journal of the American Ceramic Society*, *90*(4), 1038–1044. https://doi.org/10.1111/j.1551-2916.2007.01595.x

Flatt, R. J., Roussel, N., & Cheeseman, C. R. (2012). Concrete: An eco material that needs to be improved. *Journal of the European Ceramic Society*, *32*(11), 2787–2798. https://doi.org/10.1016/j.jeurceramsoc.2011.11.012

Flesch, J. C., Spicer, P. T., & Pratsinis, S. E. (1999). Laminar and Turbulent Shear-Induced Flocculation of Fractal Aggregates. *AiChE Journal*, *45*(5), 1114–1123.

Freitas, A. A., Santos, R. L., Colaço, R., Bayão Horta, R., & Canongia Lopes, J. N. (2015). From lime to silica and alumina: Systematic modeling of cement clinkers using a general force-field. *Physical Chemistry Chemical Physics*, *17*(28), 18477–18494. https://doi.org/10.1039/c5cp02823j

Fuchs, N. (1934). Über die Stabilität und Aufladung der Aerosole. *Zeitschrift Für Physik*, *89*(11–12), 736–743. https://doi.org/10.1007/BF01341386

Gallo-Molina, J. P., Alves de Freitas, A., Canongia Lopes, J. N., Nopens, I., & Lesage, K. (2021). Molecular dynamics simulations of effective interactions among clinker minerals in aqueous solution and the structure and dynamics of the interstitial water. *Materials and Structures*, *54*(3). https://doi.org/10.1617/s11527-021-01731-9

Gallo-Molina, J. P., Lesage, K., & Nopens, I. (2020). Numerical Validation of a Population Balance Model Describing Cement Paste Rheology. *Materials*, *13*(5), 1249. https://doi.org/10.3390/ma13051249

Ha, Z., & Liu, S. (2008). Settling Velocities of Polydisperse Concentrated Suspensions. *The Canadian Journal of Chemical Engineering*, *80*(5), 783–790. https://doi.org/10.1002/cjce.5450800501

Han, M., & Lawler, D. (1992). The (Relative) Insignificance of G in Flocculation. *Journal (American Water Works Association)*, *84*(10).

Holzer, L., Gasser, PH., Kaech, A., Wegmann, M., Zingg, A., Wepf, R., & Muench, B. (2007). Cryo-FIB-nanotomography for quantitative analysis of particle structures in cement suspensions. *Journal of Microscopy*, *227*(3), 216–228. https://doi.org/10.1111/j.1365-2818.2007.01804.x

Honig, E. P., Roebersen, G. J., & Wiersema, P. H. (1971). Effect of hydrodynamic interaction on the coagulation rate of hydrophobic colloids. *Journal of Colloid and Interface Science*, *36*(1), 97–109. https://doi.org/10.1016/0021-9797(71)90245-1

Honorio, T., Guerra, P., & Bourdot, A. (2020). Molecular simulation of the structure and elastic properties of ettringite and monosulfoaluminate. *Cement and Concrete Research*, *135*(May 2019), 106126. https://doi.org/10.1016/j.cemconres.2020.106126

Jeldres, R., Fawell, O., & Florio, B. (2018). Population balance modelling to describe the particle aggregation process: A review. *Powder Technology*, *326*, 190–207. https://doi.org/.1037//0033-2909.I26.1.78

Jeldres, R. I., Concha, F., & Toledo, P. G. (2015). Population balance modelling of particle flocculation with attention to aggregate restructuring and permeability. *Advances in Colloid and Interface Science*, *224*, 62–71. https://doi.org/10.1016/j.cis.2015.07.009

Jönsson, B., Wennerström, H., Nonat, A., & Cabane, B. (2004). Onset of cohesion in cement paste. *Langmuir*, *20*(16), 6702–6709. https://doi.org/10.1021/la0498760

Kalinichev, A. G., Wang, J., & Kirkpatrick, R. J. (2007). Molecular dynamics modeling of the structure, dynamics and energetics of mineral-water interfaces: Application to cement materials. *Cement and Concrete Research*, *37*(3), 337–347. https://doi.org/10.1016/j.cemconres.2006.07.004

Kumar, J., Peglow, M., Warnecke, G., & Heinrich, S. (2008). An efficient numerical technique for solving population balance equation involving aggregation, breakage, growth and nucleation. *Powder Technology*, *182*(1), 81–104. https://doi.org/10.1016/j.powtec.2007.05.028

Kumar, J., Peglow, M., Warnecke, G., Heinrich, S., & Mörl, L. (2006). Improved accuracy and convergence of discretized population balance for aggregation: The cell average technique. *Chemical Engineering Science*, *61*(10), 3327–3342. https://doi.org/10.1016/j.ces.2005.12.014

Lesko, S., Lesniewska, E., Nonat, A., Mutin, J. C., & Goudonnet, J. P. (2001). Investigation by atomic force microscopy of forces at the origin of cement cohesion. *Ultramicroscopy*, *86*(1–2), 11–21. https://doi.org/10.1016/S0304-3991(00)00091-7

Li, X. Y., & Logan, B. E. (2001). Permeability of fractal aggregates. *Water Research*, *35*(14), 3373–3380. https://doi.org/10.1016/S0043-1354(01)00061-6

Liu, F., Sun, Z., & Qi, C. (2015). Raman Spectroscopy Study on the Hydration Behaviors of Portland Cement Pastes during Setting. *Journal of Materials in Civil Engineering*, *27*(8), 04014223. https://doi.org/10.1061/(ASCE)MT.1943-5533.0001189

Lomboy, G., Sundararajan, S., Wang, K., & Subramaniam, S. (2011). A test method for determining adhesion forces and Hamaker constants of cementitious materials using atomic force microscopy. *Cement and Concrete Research*, *41*(11), 1157–1166. https://doi.org/10.1016/j.cemconres.2011.07.004

Ma, H., Pazmino, E., & Johnson, W. P. (2011). Surface heterogeneity on hemispheres-in-cell model yields all experimentally-observed non-straining colloid retention mechanisms in porous media in the presence of energy barriers. *Langmuir*, *27*(24), 14982–14994. https://doi.org/10.1021/la203587j

Madura, J. D., & Jorgensen, W. L. (1986). Ab initio and Monte Carlo calculations for a nucleophilic addition reaction in the gas phase and in aqueous solution. *Journal of the American Chemical Society*, *108*(10), 2517–2527. https://doi.org/10.1021/ja00270a005

Mandelbrot, B. (1982). *The Fractal Geometry of Nature*. Times Books.

MATLAB (No. R2021b). (2021). The MathWorks Inc.

Mohamed, A. R., el Kordy, A., & Elsalamawy, M. (2014). Prediction of SEM-X-ray images' data of cement-based materials using artificial neural network algorithm. *Alexandria Engineering Journal*, *53*(3), 607–613. https://doi.org/10.1016/j.aej.2014.04.007

Nachbaur, L., Nkinamubanzi, P. C., Nonat, A., & Mutin, J. C. (1998). Electrokinetic properties which control the coagulation of silicate cement suspensions during early age hydration. *Journal of Colloid and Interface Science*, *202*(2), 261–268. https://doi.org/10.1006/jcis.1998.5445

Plassard, C., Lesniewska, E., Pochard, I., & Nonat, A. (2005). Nanoscale Experimental Investigation of Particle Interactions at the Origin of the Cohesion of Cement. *Langmuir*, *21*, 7263–7270. https://doi.org/10.1021/la050440+

Puisto, A., Illa, X., Mohtaschemi, M., & Alava, M. J. (2012). Modeling the viscosity and aggregation of suspensions of highly anisotropic nanoparticles. *European Physical Journal E*, *35*(1), 1–7. https://doi.org/10.1140/epje/i2012-12006-1

Quemada, D. (1977). Rheology of concentrated disperse systems and minimum energy dissipation principle. *Rheologica Acta*, *16*(1), 82–94. https://doi.org/10.1007/BF01516932

Quemada, D. (1998). Rheological modelling of complex fluids. I. The concept of effective volume fraction revisited. *The European Physical Journal Applied Physics*, *1*(1), 119–127. https://doi.org/10.1051/epjap:1998125

Ramkrishna, D. (2000). *Population balances: Theory and applications to particulate systems in engineering*. Academic Press.

Roussel, N. (2007). Rheology of fresh concrete : from measurements to predictions of casting processes. *Materials and Structures*, *40*, 1001–1012. https://doi.org/10.1617/s11527-007-9313-2

Roussel, N., Geiker, M. R., Dufour, F., Thrane, L. N., & Szabo, P. (2007). Computational modeling of concrete flow: General overview. *Cement and Concrete Research*, *37*(9), 1298–1307. https://doi.org/10.1016/j.cemconres.2007.06.007

Roussel, N., Lemaître, A., Flatt, R. J., & Coussot, P. (2010). Steady state flow of cement suspensions: A micromechanical state of the art. *Cement and Concrete Research*, *40*(1), 77–84. https://doi.org/10.1016/j.cemconres.2009.08.026

Roussel, N., Ovarlez, G., Garrault, S., & Brumaud, C. (2012). The origins of thixotropy of fresh cement pastes. *Cement and Concrete Research*, *42*(1), 148–157. https://doi.org/10.1016/j.cemconres.2011.09.004

Runkana, V., Somasundaran, P., & Kapur, P. C. (2005). Reaction-limited aggregation in presence of short-range structural forces. *AIChE Journal*, *51*(4), 1233–1245. https://doi.org/10.1002/aic.10375

Schmid, T., & Dariz, P. (2019). Raman Microspectroscopic Imaging of Binder Remnants in Historical Mortars Reveals Processing Conditions. *Heritage*, *2*(2), 1662–1683. https://doi.org/10.3390/heritage2020102

Selomulya, C., Bushell, G., Amal, R., & Waite, T. D. (2002). Aggregation mechanisms of latex of different particle sizes in a controlled shear environment. *Langmuir*, *18*(6), 1974–1984. https://doi.org/10.1021/la010702h

Smoluchowski, M. v. (1917). Versuch einer mathematischen Theorie der Koagulationskinetik kolloider Lösungen. *Zeitschrift Für Physikalische Chemie*, *92*, 129–168. https://doi.org/10.1515/zpch-1918-9209

Struble, L., & Sun, G. K. (1995). Viscosity of Portland cement paste as a function of concentration. *Advanced Cement Based Materials*, *2*(2), 62–69. https://doi.org/10.1016/1065-7355(95)90026-8

Thiedeitz, M., Dressler, I., Kränkel, T., Gehlen, C., & Lowke, D. (2020). Effect of Pre-Shear on Agglomeration and Rheological Parameters of Cement Paste. *Materials*, *13*(9), 2173. https://doi.org/10.3390/ma13092173

Todorov, I. T., Smith, W., Trachenko, K., & Dove, M. T. (2006). DL_POLY_3: new dimensions in molecular dynamics simulations via massive parallelism. *Journal of Materials Chemistry*, *16*(20), 1911. https://doi.org/10.1039/b517931a

Uchikawa, H., Hanehara, S., & Sawaki, D. (1997). The role of steric repulsive force in the dispersion of cement particles in fresh paste prepared with organic admixture. *Cement and Concrete Research*, *27*(1), 37–50. https://doi.org/10.1016/S0008-8846(96)00207-4

Ukrainczyk, N. (2010). Kinetic modeling of calcium aluminate cement hydration. *Chemical Engineering Science*, *65*(20), 5605–5614. https://doi.org/10.1016/j.ces.2010.08.012

van Damme, H. (2006). Colloidal Chemo-Mechanics of Cement Hydrates and Smectite Clays: Cohesion Vs. Swelling. *Encyclopedia of Surface and Colloid Science*, 1411–1426. https://doi.org/10.1081/E-ESCS-120000583

van de Ven, T. G. M., & Mason, S. G. (1976). The microrheology of colloidal dispersions: IV. Pairs of interacting spheres in shear flow. *Journal of Colloid and Interface Science*, *57*(3), 505–516. https://doi.org/10.1016/0021-9797(76)90229-0

Vanni, M. (2000). Approximate population balance equations for aggregation-breakage processes. *Journal of Colloid and Interface Science*, *221*(2), 143–160. https://doi.org/10.1006/jcis.1999.6571

Vanni, M., & Baldi, G. (2002). Coagulation efficiency of colloidal particles in shear flow. *Advances in Colloid and Interface Science*, *97*(1–3), 151–177. https://doi.org/10.1016/S0001-8686(01)00050-1

Verwey, E. J. W. (1947). Theory of the Stability of Lyophobic Colloids. *The Journal of Physical and Colloid Chemistry*, *51*(3), 631–636. https://doi.org/10.1021/j150453a001

Wang, J., Kalinichev, A. G., & Kirkpatrick, R. J. (2004). Molecular modeling of water structure in nano-pores between brucite (001) surfaces. *Geochimica et Cosmochimica Acta*, *68*(16), 3351–3365. https://doi.org/10.1016/j.gca.2004.02.016

Wheeler, J., & Chatterji, S. (1972). Settling of Particles in Fresh Cement Pastes. *Journal of the American Ceramic Society*, *55*(9), 461–464. https://doi.org/10.1111/j.1151-2916.1972.tb11340.x

Wu, Y., Tepper, H. L., & Voth, G. A. (2006). Flexible simple point-charge water model with improved liquid-state properties. *The Journal of Chemical Physics*, *124*(2), 024503. https://doi.org/10.1063/1.2136877

Yeoh, G. H., Cheung, C., & Tu, J. (2014). *Multiphase flow analysis using population balance modeling*. Elsevier. https://doi.org/10.1016/B978-0-08-098229-8.00001-2

Yu, B., & Cheng, P. (2002). A fractal permeability model for bi-dispersed porous media. *International Journal of Heat and Mass Transfer*, *45*(14), 2983–2993. https://doi.org/10.1016/S0017-9310(02)00014-5

Yu, B., & Li, J. (2001). Some fractal characters of porous media. *Fractals*, *9*(3), 365–372. https://doi.org/10.1142/S0218348X01000804

Yu, B., & Liu, W. (2004). Fractal Analysis of Permeabilities for Porous Media. *AIChE Journal*, *50*(1), 46–57. https://doi.org/10.1002/aic.10004

Zingg, A., Holzer, L., Kaech, A., Winnefeld, F., Pakusch, J., Becker, S., & Gauckler, L. (2008). The microstructure of dispersed and non-dispersed fresh cement pastes — New insight by cryo-microscopy. *Cement and Concrete Research*, *38*(4), 522–529. https://doi.org/10.1016/j.cemconres.2007.11.007